Research article

Na Kong*, Li Ding, Xiaobin Zeng, Junqing Wang, Wenliang Li, Sanjun Shi, Silvia Tian Gan, Xianbing Zhu*, Wei Tao and Xiaoyuan Ji*

Comprehensive insights into intracellular fate of WS_2 nanosheets for enhanced photothermal therapeutic outcomes via exocytosis inhibition

https://doi.org/10.1515/nanoph-2019-0343
Received September 3, 2019; revised October 4, 2019; accepted October 4, 2019

Abstract: Two-dimensional (2D) nanosheet (NS)-based photothermal agents (PTAs), such as transition-metal dichalcogenides, have shown immense potential for their use in cancer photothermal therapy (PTT). However, the nano-bio interaction study regarding these NS-based PTAs is still in its infancy. In this study, we used WS_2-PEG NS-based PTA as an example to provide comprehensive insights into the experimental understanding of their fate in cancer cells. The data revealed that three different endocytosis pathways (macropinocytosis, clathrin-dependent, and caveolae-dependent endocytosis), autophagy-mediated lysosome accumulation, and exocytosis-induced excretion contribute to the integrated pathways of WS_2-PEG NSs within cells. These pathways are consistent with our previous reports on MoS_2-PEG NS-based drug delivery platform, indicating that the composition difference of 2D NSs with PEGylation may have little influence on their intercellular fate. Moreover, by blocking the revealed exocytosis pathway-mediated secretion of WS_2 NSs in tumor cells, an effective approach is proposed to attain enhanced photothermal therapeutic outcomes with low doses of WS_2 NSs and under a low power of a near-infrared (NIR) laser. We expect that the exocytosis inhibition strategy may be a universal one for 2D NSs to achieve combination cancer therapy. This study may also provide more experimental basis for the future development of 2D NS's application in biomedicine (e.g. PTT).

Keywords: WS_2 nanosheets; photothermal agents; intracellular fate; exocytosis inhibition; enhanced photothermal therapy.

1 Introduction

Two-dimensional (2D) materials, such as transition-metal dichalcogenide nanosheets (TMD NSs), black phosphorus NSs, MXene, and so on, have shown promising achievements in various biomedical applications including cancer photothermal therapy (PTT) [1–15]. Although impressive breakthroughs of these TMD NSs in the application of PTT have been preliminarily achieved [16, 17], their safety and impact on patient health still remains a big problem to be addressed [18–21].

The safety issue is closely related to the nano-bio interactions between the nanomaterials and the biosystem [22–24]. The intracellular fate of the nanomaterials (e.g. internalization, intracellular trafficking, and excretion) is one of the most important nano-bio interactions that is closely related to their safety issues [25–27]. Moreover, as these activities occur also toward the end period of their journey in the biosystem, they are usually crucial factors in determining the final therapeutic effects of various modalities of 2D material-based

---

***Corresponding authors: Na Kong,** School of Medicine, Zhejiang University, Hangzhou 310012, Zhejiang, China, e-mail: kongna@zju.edu.cn; **Xianbing Zhu,** Department of Biochemistry, Rosalind and Morris Goodman Cancer Research Center, McGill University, Montreal, Quebec H3A 1A3, Canada; and School of Life Sciences, Tsinghua University, Beijing 100084, China, e-mail: xianbing.zhu@mail.mcgill.ca; and **Xiaoyuan Ji,** Center Lab of Longhua Branch, and Department of Infectious Disease, Shenzhen People's Hospital, 2nd Clinical Medical College of Jinan University, Shenzhen 518120, Guangdong Province, China; and Brigham and Women's Hospital, Harvard Medical School, Boston, MA 02115, USA, e-mail: jixiaoyuan007@163.com
Li Ding: School of Life Sciences, Tsinghua University, Beijing 100084, China
Xiaobin Zeng: Center Lab of Longhua Branch, and Department of Infectious Disease, Shenzhen People's Hospital, 2nd Clinical Medical College of Jinan University, Shenzhen 518120, Guangdong Province, China
Junqing Wang, Wenliang Li, Sanjun Shi, Silvia Tian Gan and Wei Tao: Brigham and Women's Hospital, Harvard Medical School, Boston, MA 02115, USA. https://orcid.org/0000-0002-4277-3728 (W. Tao)

nanotherapeutics (e.g. PTT, drug delivery platforms for chemotherapy or gene therapy, etc.) [25–30]. However, systematic experimental studies of the intracellular fate of the 2D NSs still remain rare and largely unexplored up to now [21, 24, 25].

Recently, we have carried out, for the first time, pioneering systematic experimental studies on the intracellular fate of 2D MoS_2 NSs in cancer cells and their application in drug delivery platform-based anti-exocytosis-enhanced cancer treatment [27]. A fluorescent chemotherapeutic drug (i.e. doxorubicin) was tightly loaded on the surface of 2D MoS_2 NSs, and immunofluorescence co-localization analysis was used to obtain a cellular-level understanding of the 2D MoS_2-based drug delivery platform's fate in different cells. However, as few reports have revealed the intercellular fate of 2D NSs up to now, it is still unclear whether the composition difference of the 2D NSs could affect their fate within the cells. Moreover, it is also to be determined whether the reported exocytosis inhibition strategy for enhanced cancer therapy could be a universal one for other therapeutic modalities (e.g. single photothermal agents (PTAs) for PTT) to achieve combination cancer therapy.

In order to address the above remaining questions and provide a strong basis for systematic experimental studies of the intracellular fate of the 2D NSs, we chose WS_2, another well-known member of 2D TMDs [31] that has a composition different from that of MoS_2, as a model 2D NS in this study. The intracellular fate of WS_2 NS-based PTAs was revealed via rhodamine (RB)-conjugated PEGylated WS_2 NSs through the immunofluorescence co-localization analysis used in our previous reports [26, 27]. Two common cancer cell lines, namely HeLa (human cervical cancer cells) and MCF-7 (human breast cancer cells), were used as model cancer cells. The co-localizations between different intracellular vesicle markers (endocytosis, autophagy, and exocytosis) and WS_2 NSs were detected to systematically investigate the cell-level activities of these WS_2 NSs. Various pharmacological inhibitors targeting different transport pathways were also used to further verify the results. Our results demonstrated that the composition difference of PEGylated NSs has little influence on the reported pathways of these 2D NSs (i.e. through the same pathways as were confirmed in our previous report) [27]. In addition, the exocytosis inhibition strategy could also improve the therapeutic efficacy (photothermal therapeutic outcomes) of WS_2 NS-based PTAs (with a low dose of WS_2 NSs and under a near-infrared (NIR) laser with low power). Therefore, the exocytosis inhibition strategy might be a universal method for 2D NSs to achieve combination cancer therapy, which can not only derive the maximum therapeutic benefits but also limit their adverse health effects caused by overdose of materials.

2 Materials and methods

2.1 Materials

N-butyllithium, hexane, lipoic acid (LA), *N*,*N*-dicyclohexylcarbodiimide (DCC), WS_2 powder, triethylamine (TEA), and MTT were obtained from Sigma-Aldrich. Rhodamine PEG amine (RB-PEG-NH_2) and mPEG-LA were obtained from Nanocs (New York, NY, USA). LC3 and LAMP1 antibodies were obtained from CST (Cell Signaling Technology, Inc., Danvers, MA, USA). The β-actin antibody was purchased from Abmart, Inc. (Berkeley Heights, NJ, USA)

2.2 RB-mPEG-LA synthesis

In brief, RB-mPEG-NH_2 was reacted with LA at the molar ratio of 1:2 in 2 ml dichloromethane (DCM; pre-dissolving 6 μL TEA and 10 mg of DCC) for 24 h. Ten milliliters of water was then added into the bottle after the final solution was blown-dried by N_2. After removing the insoluble solid, the solution pH was adjusted to 8. DCM was used to extract the filtrate solution (three times). The final products were dissolved in H_2O and then lyophilized after evaporation of the organic solvent.

2.3 WS_2 NSs synthesis and PEG coating

WS_2 NSs were prepared as previously reported [31]. In brief, we used *n*-butyllithium (1.6 M in hexane, 10 ml) to disperse the WS_2 powder (50 mg). After the intercalation by lithium by 2 days of stirring, the WS_2 cloudy dispersion was centrifuged at 5000 rpm and washed three times with 100 ml hexane to get rid of excessive lithium with some other organic residues. The intercalated WS_2 materials were immersed in deionized (DI) water (30 ml), and then liquid exfoliation was performed through 5 h of sonication. Unexfoliated WS_2 was removed by centrifugation at 5000 rpm. Membranes of 14 kDa molecular weight cut-off (MWCO) were used to get rid of the residual ions, and the obtained WS_2 was then dispersed in H_2O. To coat a layer of PEG, WS_2 NSs (10 mg) were dissolved in DI water (10 ml) with 50 mg of pre-dissolved LA-PEG. Then the samples were ultrasonicated for 30 min and stirred overnight. Filters of 100 kDa MWCO were used to remove the excess

LA-PEG via centrifugal filtration. The obtained WS_2-PEG samples were washed several times and finally resuspended in DI water.

2.4 Fluorescence marking of PEGylated WS_2 NSs

For rhodamine marking, WS_2 NSs (10 mg) were suspended in DI water (10 ml) containing 25 mg of pre-dissolved LA-PEG and 25 mg of LA-PEG-RB. Then the samples were ultrasonicated for 30 min and stirred overnight. Filters of 100 kDa MWCO were used to remove the excess LA-PEG and LA-PEG-RB via centrifugal filtration. The obtained WS_2-PEG samples were washed several times and finally resuspended in DI water.

2.5 Characterization

TEM (transmission electron microscopy, JEM-2100UHR, Japan) and AFM (atomic force microscopy, FASTSCANBIO, Germany) were used to characterize the morphology of WS_2-PEG NSs. UV-vis-NIR absorption spectra of WS_2-PEG NSs and WS_2-PEG-RB NSs were obtained by a plate reader (Infinite® 200 PRO, Tecan Trading AG, Switzerland). Energy dispersive spectroscopy (EDS) and X-ray photoelectron spectroscopy (XPS) (ESCALAB 250Xi, Japan) were used to analyze the compositions of the WS_2-PEG NSs.

2.6 Calculation of extinction coefficient

The extinction coefficient of WS_2-PEG NSs was determined according to the Beer-Lambert law. Detailed calculation was as follows:

$$\varepsilon_{808} = \frac{A_{808}}{CL},$$

where ε is the extinction coefficient, A_{808} is the absorption at the wavelength of 808 nm of WS_2-PEG NSs, L is the path length (cm), and C (g L^{-1}) is the concentration of the WS_2-PEG NSs.

2.7 Measurement of photothermal performance

Different concentrations of WS_2-PEG NSs (0. 1, 0.2, and 0.3 mg ml^{-1}) were irradiated with an NIR laser (808 nm, 0.5 W cm^{-2}, 5 min). The temperature changes of WS_2-PEG NSs solutions were monitored by an IR thermal camera.

2.8 Cell culture

Dulbecco's Modified Eagle Medium (DMEM, with 10% of heat-inactivated fetal bovine serum (FBS)) was supplemented to culture MCF-7 and HeLa cells in this study. An incubator was used to keep both cell lines at 37°C (5% CO_2 atmosphere).

2.9 Biocompatibility assay of Exo1 *in vitro*

The cytotoxicity of Exo1 in different cell lines was tested by MTT assay. Briefly, Exo1 was added in 96-well plates (pre-seeded with the cells overnight) with the indicated concentrations for 24 h. MTT was then added (concentration: 2 mg ml^{-1}) and the cells were cultured for 4 h. Finally, cell viability was recorded by a plate reader ($\lambda = 490$ nm).

2.10 Cellular uptake of WS_2-PEG-RB NSs

Plasmid transfection, immunofluorescence studies, and intracellular fluorescence assays were performed according to our previous report [27]. WS_2-PEG-RB NSs (10 μg ml^{-1}) was used to incubate the GFP- or EGFP-Rabs transfected cells (37°C, 5% CO_2 atmosphere, 3 h). After washing three times with phosphate-buffered saline (PBS), 4% of paraformaldehyde was used to fix the cells (15 min). The images of WS_2-PEG-RB NS internalization were recorded by confocal laser scanning microscopy (CLSM).

2.11 *In vitro* toxicity assays

Cells (density: 5000 cells/well) were pre-seeded in 96-well plates, followed by 2-h incubation of nystatin, chlorpromazine, rottlerin, sucrose, or Exo1 at the indicated concentrations. The *in vitro* viability was examined by MTT assay.

2.12 Enhanced photothermal therapeutic outcomes via blocking exocytosis *in vitro*

For studying *in vitro* enhanced PTT via blocking the exocytosis of WS_2-PEG NSs, cells were treated differently at 1, 2, or 3 h as follows. Group 1: saline; Group 2: Exo1; Group 3: WS_2-PEG NSs; Group 4: Exo1 + NIR; Group 5: WS_2-PEG NSs + NIR; and Group 6: WS_2-PEG NSs + Exo1 + NIR. The concentration of WS_2 was 100 μg ml^{-1}, while the concentration of Exo1 was 50 μg ml^{-1}. NIR irradiation was carried out at the power density of 0.5 W cm^{-2} (5 min). Cells were pretreated with Exo1 for 2 h before the treatments. Afterward, the *in vitro* viability was examined by MTT assay.

2.13 Enhanced photothermal therapeutic outcomes via blocking exocytosis *in vivo*

A mice model with MCF-7 xenograft tumors was established strictly according to our previous report [24]. When the volume reached ~100 mm^3, MCF-7 breast tumor-bearing nude mice were grouped (five mice each group) and treated differently as follows. Group 1: saline; Group 2: Exo1; Group 3: WS_2-PEG NSs; Group 4: Exo1 + NIR; Group 5: WS_2-PEG NSs + NIR; and Group 6: WS_2-PEG NSs + Exo1 + NIR. We intravenously injected saline and WS_2-PEG NSs (6 mg kg^{-1}) through the tails and intratumorally injected Exo1 (4 mg kg^{-1}). The NIR irradiation (808 nm, 0.5 W/cm^2, 10 min) was done within the tumor sites after different times of WS_2-PEG NSs injection (24, 48, 72, or 120 h). The size of the tumors and the body weight of each mouse were recorded every 2 days for 2 weeks.

2.14 Hematoxylin and eosin (H&E) stained histology

A high dose of WS_2-PEG NSs (10 mg kg^{-1}) and Exo1 (10 mg kg^{-1}) was given to healthy Balb/c mice by intravenous injections. The mice were humanely sacrificed 1 month after treatment. The organs were carefully collected, fixed (10% formalin), and embedded (paraffin), followed by sections for H&E staining.

2.15 Statistics

Differences between different groups were compared by Student's t-test. The data are presented as mean ± SEM in these studies (*, $p < 0.05$; **, $p < 0.01$; ***, $p < 0.001$).

3 Results and discussion

3.1 Synthesis and characterization of PEGylated WS_2 NSs

A modified chemical exfoliation protocol with high yield was applied to prepare the 2D WS_2 NSs from bulk WS_2 according to a recently reported method [31], which is shown in Figure 1A. According to previous reports [31], the two sulfur atoms in the LA moiety enabled much stronger binding to TMDs compared to the use of a single thiol or other groups. The prepared WS_2 NSs were coated by LA-PEG (i.e. lipoic acid-conjugated PEG) to improve their dispersability, stability, and biocompatibility. AFM and TEM were used to characterize the morphology of LA-PEG-functionalized 2D WS_2 NSs. According to TEM and AFM analyses, the liquid-exfoliated PEGylated WS_2 (WS_2-PEG) NSs were ~120 nm in size and ~3.5 nm in thickness (Figure 1B–D). The chemical composition of 2D WS_2-PEG NSs was further confirmed by XPS and STEM-EDS mapping. As shown in Figures S1 and 1E, there were characteristic WS_2 peaks and additional LA-PEG peaks in the XPS spectra, and the elements W, S, C, N, and O could be seen in EDS mapping. All indicated the successful functionalization of WS_2 with LA-PEG. The extinction coefficient (ε) was calculated to be 21.34 L g^{-1} cm^{-1} (Figure S2). The strong NIR absorption and high ε value of WS_2-PEG NSs demonstrate the great potential of WS_2-PEG NSs acting as an efficient photothermal agent under 808-nm laser illumination. Then the photothermal effect of WS_2-PEG NSs was examined by exposing aqueous solutions containing WS_2-PEG NSs (0–300 μg ml^{-1}) to an 808-nm NIR laser (0.5 W cm^{-2}) and characterized by an IR thermal camera. The photothermal heating curves (Figures 1F and S3) show that the photothermal effect of WS_2-PEG NSs is concentration-dependent with the highest temperature increase of up to ~43°C after 5 min of NIR laser treatment. However, the temperature of H_2O increased only ~4°C at the same test level.

3.2 Fluorescence marking of WS_2-PEG NSs

For tracking the intracellular trafficking network of WS_2 NSs, a fluorescent probe, rhodamine B (RB), was labeled on the surface of WS_2 NSs through reaction with LA-PEG-RB. As shown in Figure 1G, the characteristic absorbance peak of RB ($\lambda = 550$ nm) was verified through the UV-vis-NIR spectrum of WS_2-PEG-RB NSs, after removing the excess LA-PEG-RB by centrifugal filtration.

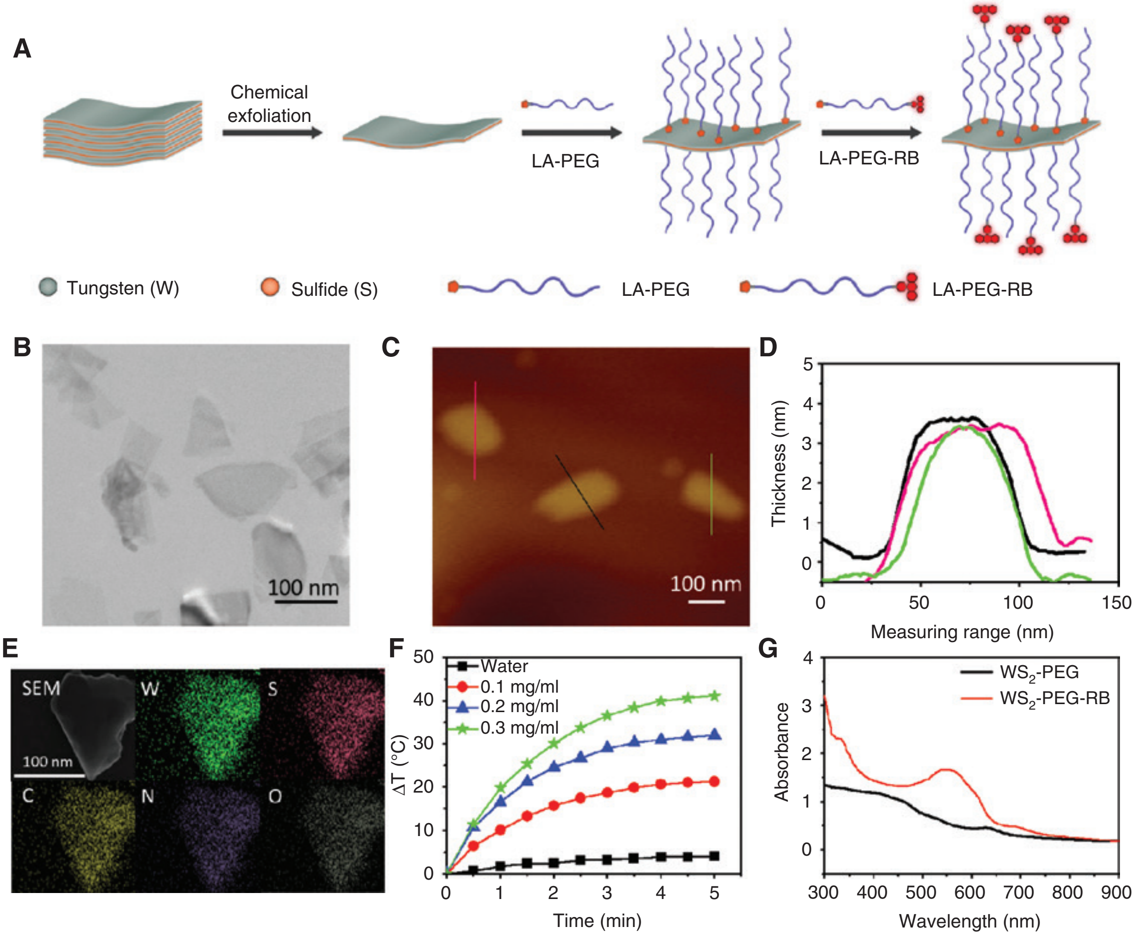

Figure 1: Synthesis and characterization of WS$_2$-based NSs.
(A) Schematic diagram of the synthesis of WS$_2$-based NSs. (B) TEM images of WS$_2$-PEG NSs. (C) AFM images of WS$_2$-PEG NSs. (D) Thickness of WS$_2$-PEG NSs. (E) STEM-EDC mapping of WS$_2$-PEG NSs. (F) Photothermal heating curves of the WS$_2$-PEG solution at different concentrations (0.1, 0.2, and 0.3 mg ml^{-1}) and water under NIR irradiation (808 nm, 0.5 W cm^{-2}). (G) Absorbance spectra of WS$_2$-PEG and WS$_2$-PEG-RB NSs.

3.3 Energy-dependent internalization

As a therapeutic or diagnostic agent for cancer, the internalization and subsequent retention of the agent is the key to the potency of the treatment. MCF-7 and HeLa cells were chosen as model cell lines. The ingestion and location of fluorescent WS$_2$-PEG-RB NSs were examined through CLSM, as shown in Figure 2A, where the NSs were observed to localize in the cytoplasm in both cell lines. The fluorescence density of NSs in these two cells lines increased with time (Figures 2B,C and S4), indicating sustained uptake of WS$_2$-PEG-RB NSs. Unlike small molecules that enter cells by passive diffusion, the internalization of nanomaterials may need an energy-dependent pathway such as endocytosis. In order to verify this, we incubated WS$_2$-PEG-RB NSs with cells under different temperatures, namely 37 and 4°C, for 2 h. The endocytosis of nanomaterials could be affected by temperature because low temperature kills the activity of the proteins involved in endocytosis. As observed in Figure 2D–F, cellular uptake of WS$_2$-PEG-RB NSs significantly reduced at the lower temperature. In order to further confirm the role of energy depletion on cellular uptake, two metabolic inhibitors, namely bafilomycin A (inhibiting the function of v-ATPase) and sodium azide (depleting the ATP within cells), were applied in our further experiments. Pretreatment with these two metabolic inhibitors notably suppressed the cellular uptake of WS$_2$-PEG-RB NSs (Figure S5), suggesting that the internalization was indeed energy-dependent.

3.4 Endocytosis pathways

In general, there are several different endocytosis pathways for nanomaterials to enter cancer cells, including caveolae-dependent endocytosis, clathrin-dependent

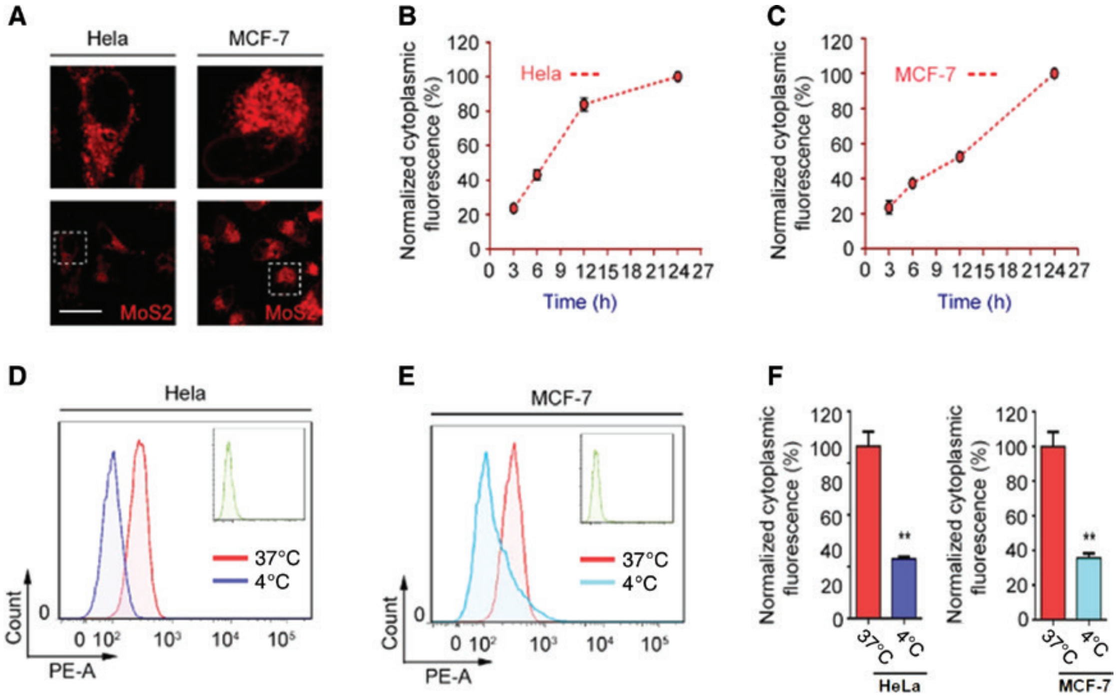

Figure 2: Effect of temperature on the internalization of WS2-based NSs.
(A) The ingested fluorescence of WS_2-based NSs was monitored by CLSM after 2-h incubation. The enlarged images are shown in the top row. Scale bars: 10 μm. The dynamic internalization of fluorescent WS2-NSs was monitored by flow cytometer and quantified in (B) HeLa cells and (C) MCF-7 cells. Effect of temperature (37 and 4°C) on WS2-based NSs' uptake was measured by flow cytometer after 2 h incubation in (D) HeLa cells and (E) MCF-7 cells. (F) The cytoplasmic fluorescence was statistically analyzed. Scale bars: 10 μm.

endocytosis, caveolae-independent endocytosis, clathrin-independent endocytosis, and micropinocytosis [26, 27]. There are also several biomarkers for each endocytosis pathway. For example, Afr6, RhoA, Cdc42, and flotillin are involved in caveolae- and clathrin-independent endocytosis, and Rab34 is considered to be a biomarker for macropinocytosis [32, 33]. In order to reveal the pathways taken by WS_2-based NSs to enter the cells, the cells were first transfected with EGFP-caveolin, clathrin, flotillin, RhoA, Rab34, Cdc42, and Arf6 to mark each pathway. Then the marked cells were treated with WS_2-PEG-RB NSs for 2 h. NS-containing vesicles got co-localized with caveolin-, clathrin-, and Rab34-positive vesicles (Figures 3A–C and S6). In contrast, there was no observable co-localization of WS_2-based NSs with flotillin-, RhoA-, Cdc42-, and Arf6-positive vesicles (Figures S7 and S8). All the CLSM images indicate that the caveolin-dependent and clathrin-dependent endocytosis and macropinocytosis were the predominant pathways for the internalization of WS_2 NSs. In order to further confirm these pathways and to distinguish the contribution from each endocytic pathway, pharmacological inhibitors of individual endocytosis pathway were employed to block the confirmed pathways above. Chlorpromazine and sucrose were applied to suppress clathrin-mediated endocytosis [34], and nystatin and rottlerin were used to inhibit caveolae-dependent endocytosis and micropinocytosis, respectively [35]. After 2 h of incubation with different inhibitors, the cells were exposed to WS_2-PEG-RB NSs for an additional 3 h. The cytoplasmic fluorescence was measured (Figure 3D). These inhibitors did not influence the cellular metabolic activity of the cells (Figures S9 and S10). Nevertheless, the uptake of NSs evidently decreased after incubation with these inhibitors. For example, after blocking caveolae-dependent endocytosis using nystatin, the cell uptake of NSs drastically reduced, with only 50% of the fluorescent NS signal being observed in cells. Likewise, chlorpromazine and sucrose, the clathrin-dependent pathway inhibitors, blocked about 50% of the uptake of fluorescent NSs in the two cell lines. Rottlerin suppressed approximately 30% of the uptake of fluorescent NSs in the cells. These data confirmed that caveolin-dependent, clathrin-dependent, and macropinocytosis pathways play important roles in internalizing WS_2 NSs in cancer cells and that caveolin-dependent endocytosis makes the greatest contribution to the internalization of WS_2-based NSs.

3.5 Lysosome accumulation

Generally, nanomaterials taken up by endocytosis are delivered to early endosomes first, then late endosomes,

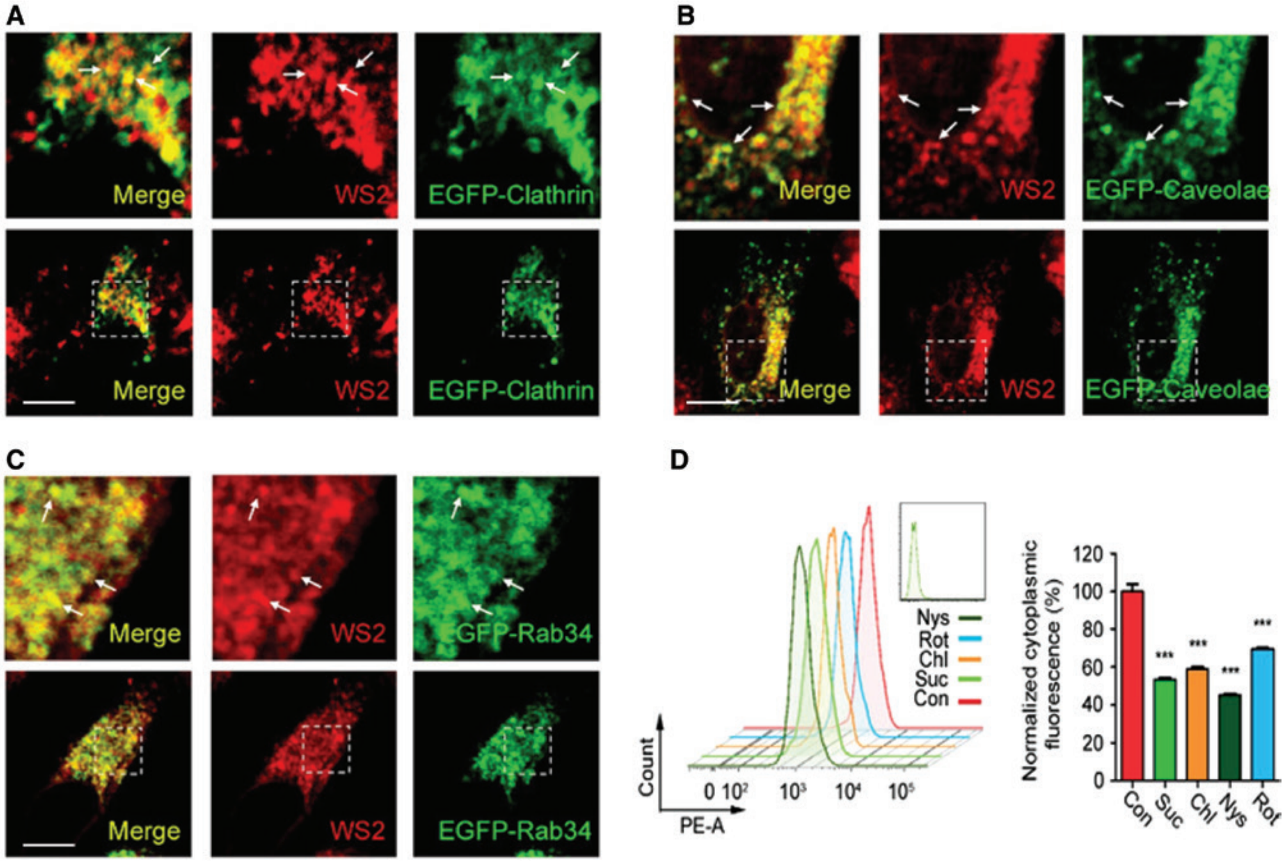

Figure 3: Endocytosis pathways of WS$_2$-based NSs.
(A) HeLa cells were transfected with EGFP-clathrin plasmid, and then the cells were incubated with WS$_2$-PEG/RB NSs for 2 h. The co-localization was determined by CLSM. (B) HeLa cells were transfected with EGFP-caveolae plasmid, and then the cells were incubated with WS$_2$-PEG/RB NSs for 2 h. The co-localization was determined by CLSM. (C) HeLa cells were transfected with EGFP-Rad34 plasmid, and then the cells were incubated with WS$_2$-PEG/RB NSs for 2 h. The co-localization was determined by CLSM. (D) HeLa cells were first treated with different inhibitors (rottlerin, 2.6 μg ml^{-1}; sucrose, 100 mg ml^{-1}; chlorpromazine, 8 μg ml^{-1}; nyatatin, 100 μg ml^{-1}) for 2 h. Then the cells were incubated with WS$_2$-PEG/RB NSs for another 3 h. The cytoplasmic fluorescence was determined by flow cytometer. Scale bars: 10 μm.

and followed by the lysosomes through the classical pathway. Rab GTPases, such as Rab5 and Rab7, are well-established markers of early endosomes and late endosomes, respectively, which can be used to identify these intracellular trafficking vesicles. Therefore, we examined the co-localization of WS$_2$-PEG-RB NSs with these markers in EGFP-Rab5 and EGFP-Rab7 overexpressed cells. WS$_2$-PEG-RB NSs co-localized well with early endosomes and late endosomes after 2 h of incubation (Figures 4B,C and S11B,C). Moreover, WS$_2$-PEG-RB NSs also perfectly merged with the lysosomes, which was identified by the lysosome marker protein Lamp1 (Figures 4D, S11D). Therefore, the data indicate that WS$_2$-PEG-RB NSs were delivered to early endosomes first, and then transported to late endosomes, followed by their accumulation in lysosomes after endocytosis-mediated internalization (Figure 4A). For the macropinocytosis pathway, however, Rab5-labeled early endosomes did not co-locate with Rab34-marked macropinosomes (Figure S12A). On the contrary, macropinosomes preferred to merge with late endosomes (Figure S12B). These data suggest that the pathway “macropinocytosis → late endosomes → lysosomes” is responsible for the turnover of WS$_2$ NSs in cancer cells.

3.6 Intracellular trafficking of WS$_2$-based NSs mediated by autophagy

Some previous studies have revealed that autophagy plays a crucial role in sequestering intracellular nanomaterials in autophagosome and delivering them to lysosomes [26, 36, 37]. Therefore, we tested the potential function of autophagy in regulating WS$_2$ NSs trafficking in cancer

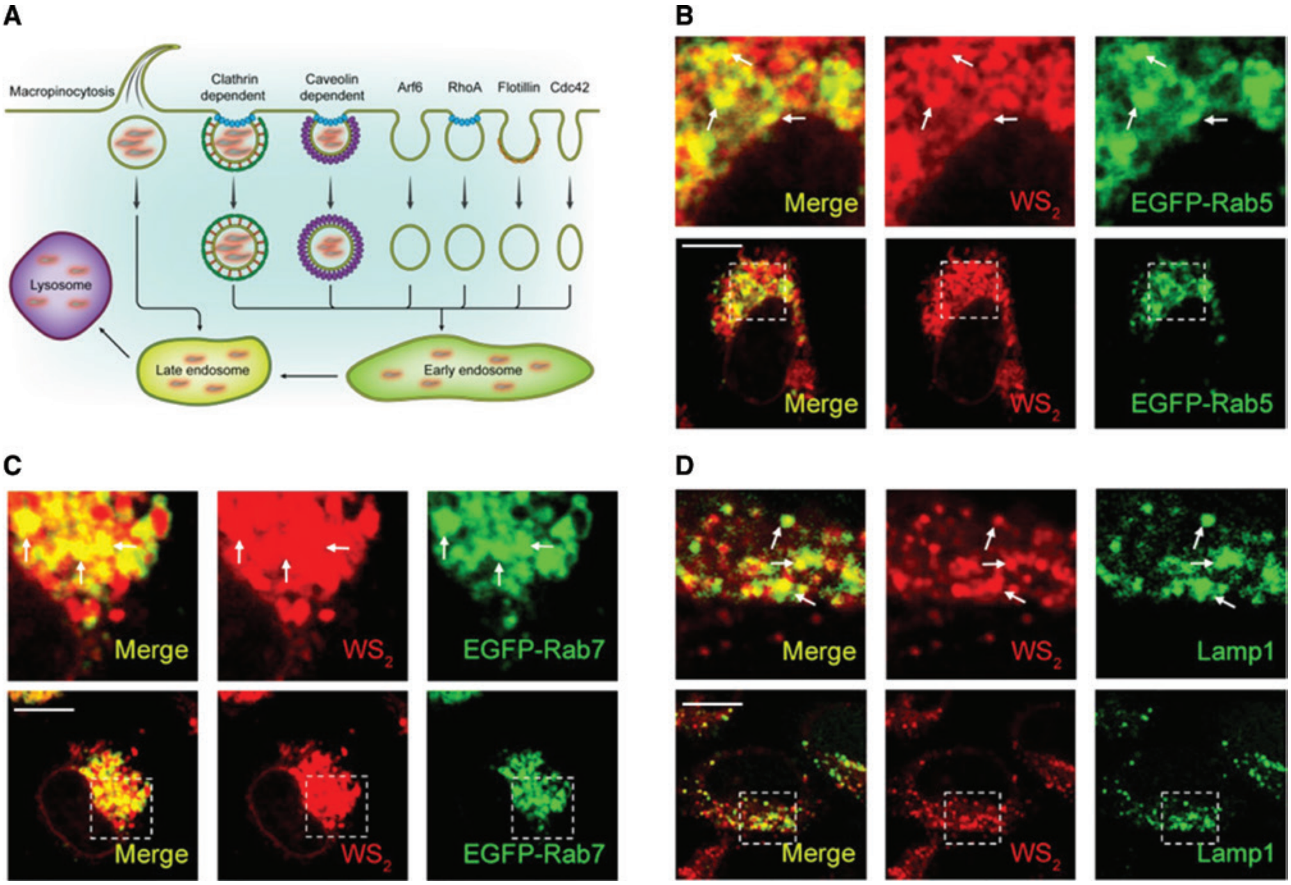

Figure 4: Accumulation of WS_2 NSs in lysosome.
Schematic diagram of internalization pathways of WS_2 NSs in (A) HeLa cells. (B) HeLa cells were transfected with EGFP-Rab5 plasmid, and then the cells were incubated with WS_2-PEG/RB NSs for 2 h. The co-localization was determined by CLSM. (C) HeLa cells were transfected with EGFP- Rad7 plasmid, and then the cells were incubated with WS_2-PEG/RB NSs for 2 h. The co-localization was determined by CLSM. (D) HeLa cells were first incubated with WS_2-PEG/RB NSs for 2 h, and then the immunofluorescence experiment was carried out to examine the co-localization between lysosome and WS_2-PEG/RB NSs. The antibody targeting Lamp1 was used to identify lysosome. Scale bars: 10 µm.

cells. After incubating with WS_2-PEG-RB NSs for 20 h, the co-localization between these NSs and LC3-positive autophagosomes was tested. As shown in Figure 5A,B, WS_2 NSs were trapped in LC3-positive autophagosomes. We also found that WS_2-based NSs could promote autophagosome formation. The LC3II proteins, which are produced and transferred on the membrane of autophagosomes when autophagy is initiated, increased after incubating with WS_2-based NSs for 20 h (Figure 5C). These data indicate that autophagy plays a pivotal role in sequestering intracellular WS_2-based NSs. Then we further examined whether autophagosome would deliver the sequestered WS_2-based NSs to lysosomes. The EGFP-LC3 transfected cells were incubated with WS_2-PEG-RB NSs for 20 h. The lysosome was labeled with a primary antibody against Lamp1. We found that WS_2-PEG-RB NSs co-localized well with both EGFP-LC3 positive autophagosome and Lamp1-labeled lysosome (Figure 5D,E), indicating that autophagosome-captured WS_2 NSs would be further delivered to the lysosome.

3.7 Exocytosis pathways

Cells swallow the nanomaterials surrounding them by endocytosis; on the other hand, exocytosis confers the cells with the ability to throw the ingested contents out of them by some specific secretory vesicles. Rab3 and Rab26 are the identity markers of the classic secretory vesicles, while Rab8 and Rab10 are used to mark the GLUT4 translocated vesicles in the secretion process [32, 38]. For investigating the possibility for the exocytosis of WS_2-PEG NSs, these NSs were added and cultured with EGFP-Rab3-, Rab26-, Rab8, and Rab10-overexpressed cells for 2 h. As presented in Figures 6A–D and S13A–D, Rab26- and Rab3-labeled classic secretory vesicles co-localized well with

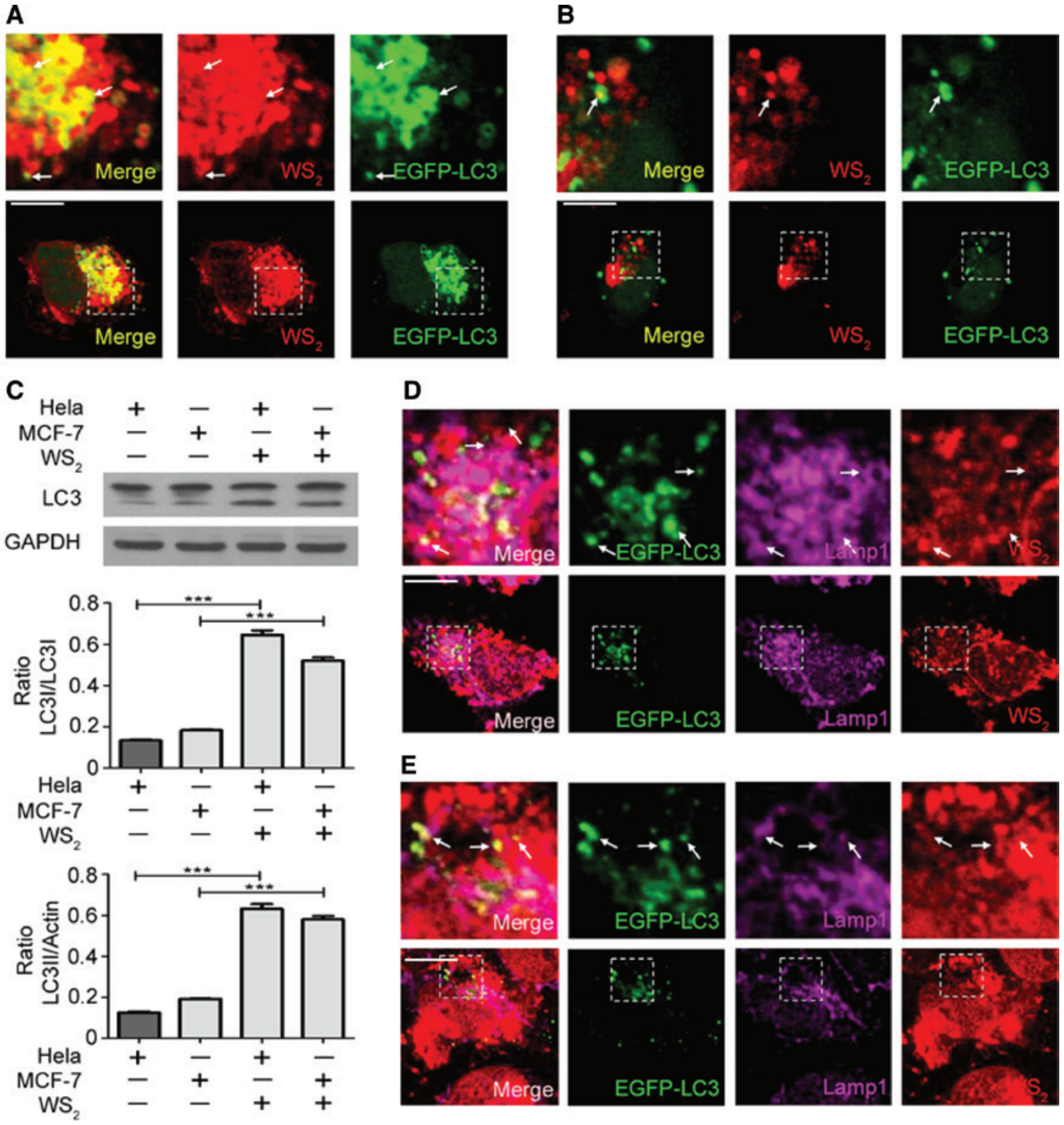

Figure 5: Autophagy contributes to WS_2 NS accumulation in the lysosome. The co-localization was determined by CLSM images (scale bar, 10 μm).
(A) HeLa cells or (B) MCF-7 cells were transfected with EGFP-LC3 plasmid, and then cultured with WS_2-PEG-RB NSs (20 h). (C) HeLa cells or MCF-7 cells were treated with NSs for 20 h. Then, the protein was collected from cells, and the protein levels of LC3 were examined by WB. The quantification of the blot was tested by the software Image J. (D) HeLa cells or (E) MCF-7 cells were first transfected with EGFP-LC3 plasmid, and then cultured with WS_2-PEG-RB NSs. Twenty hours later, the immunofluorescence assays were conducted to examine the co-localization between lysosome, autophagosome, and WS_2-PEG-RB NSs. The antibody targeting Lamp1 was used to identify lysosome.

WS_2-PEG-RB NSs. Similar results were also observed for Rab10- and Rab8-marked GLUT4 translocated vesicles, suggesting that these vesicles take part in mediating the exocytosis of WS_2 NSs. Because all these vesicles are manufactured within the Golgi body [32], we assume that WS_2 NSs are first delivered into the Golgi, followed by sorting by both the classic secretory vesicles and GLUT4 translocated vesicles. In addition, Rab24- and Rab22-positive vesicles take part in the transfer of contents from the early/late endosomes to the Golgi body [32]. Therefore, we tested whether these vesicles contribute to the delivery of WS_2 NSs from the endosomes to the Golgi. After 2 h of incubation with WS_2-PEG-RB NSs, the co-localization between the Rab22/24-positive vesicles and WS_2 NSs was examined. We could clearly observe that both early/late endosomes and WS_2-PEG-RB NSs co-localized well with

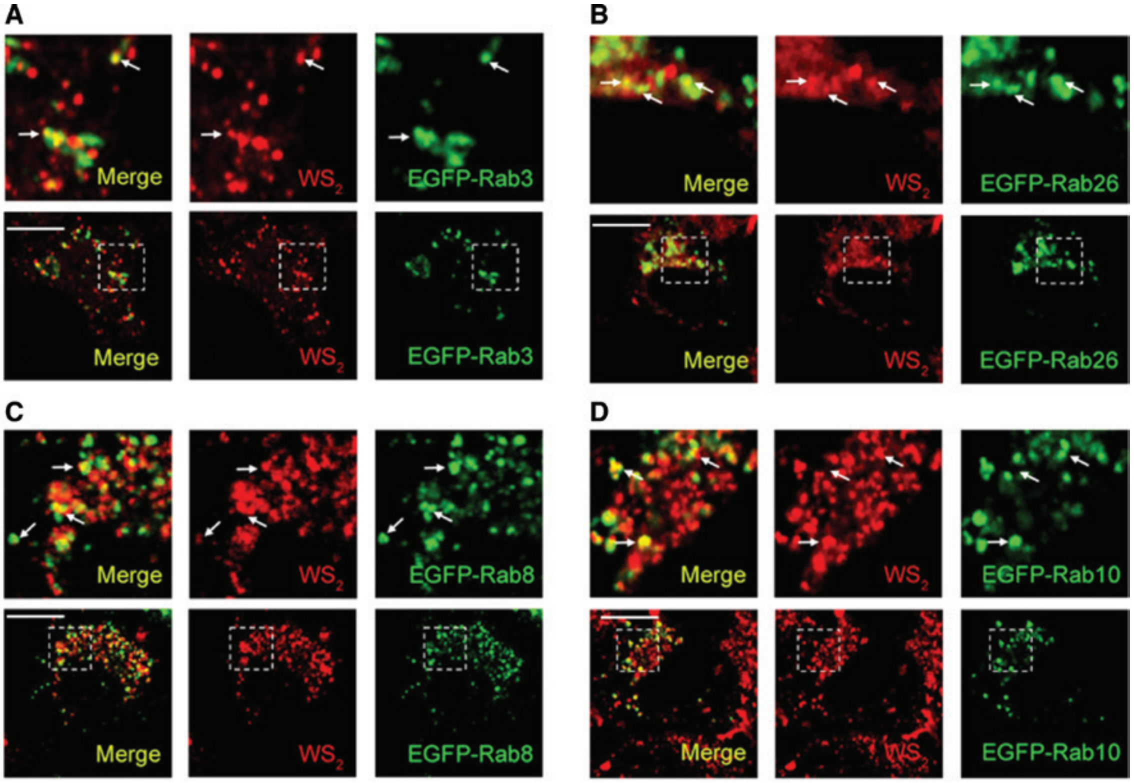

Figure 6: Exocytosis-mediated secretion of WS2 NSs.
(A) HeLa cells were transfected with EGFP-Rab3 plasmid, and then the cells were incubated with WS2-PEG/RB NSs for 2 h. The co-localization was determined by CLSM. (B) HeLa cells were transfected with EGFP-Rab26 plasmid, and then the cells were incubated with WS2-PEG/RB NSs for 2 h. The co-localization was determined by CLSM. (C) HeLa cells were transfected with EGFP-Rab8 plasmid, and then the cells were incubated with WS_2-PEG/RB NSs for 2 h. The co-localization was determined by CLSM. (D) HeLa cells were transfected with EGFP-Rab10 plasmid, and then the cells were incubated with WS_2-PEG/RB NSs for 2 h. The co-localization was determined by CLSM. Scale bars: 10 μm

Rab22/24-positive vesicles (Figure S14). These results indicate that Golgi might receive WS_2 NSs from early and late endosomes, followed by the excretion of these NSs into the extracellular space with the help of classic and GLUT4 translocated vesicles.

3.7.1 Increased accumulation of WS_2 NSs within cells via exocytosis inhibition

The exocytosis of WS_2 NSs could lead to the decreased accumulation of NSs within the cells, which may further affect the therapeutic efficacy. Enhanced accumulation of WS_2 NSs in cells can occur if exocytosis is blocked using exocytosis inhibitors (Figure 7A). Exo1, i.e. 2-(4-fluorobenzoylamino)-benzoic acid methyl ester, has been reported to be an inhibitor for exocytosis, which induces the collapse of the Golgi body's structure and functions [27]. In this study, we tested whether the accumulation of WS_2-based NSs could be increased by using Exo1 to inhibit the exocytosis pathway. After pretreatment with Exo1, the cytoplasmic fluorescence of WS_2-PEG-RB NSs increased up to 25% in HeLa cells and 35% in MCF-7 cells after 3 h of incubation of WS_2-PEG-RB NS (Figures 7B and S15A), which suggested that the accumulation of these NSs within cells could be increased by inhibiting the exocytosis pathway via Exo1. To further validate this process, we refreshed the medium of WS_2-PEG-RB NSs incubated cells and then kept the cells in culture with or without Exo1 for another 3 h. A dramatic decrease of cytoplasmic fluorescence was observed after refreshing the medium. However, Exo1 treatment could recover more than 20% loss of fluorescent NSs (Figures 7C and S15B). This result showed that the retention and accumulation of WS_2-based NSs can be increased by blocking exocytosis via Exo1.

3.7.2 Enhanced photothermal therapeutic outcomes via blocking exocytosis *in vitro*

The endocytosis and exocytosis pathways of WS_2-PEG NSs were all explored and are summarized in Figure 8A. As can be concluded from these results, the endocytosis and exocytosis pathways of WS2-PEG NSs were the same as the

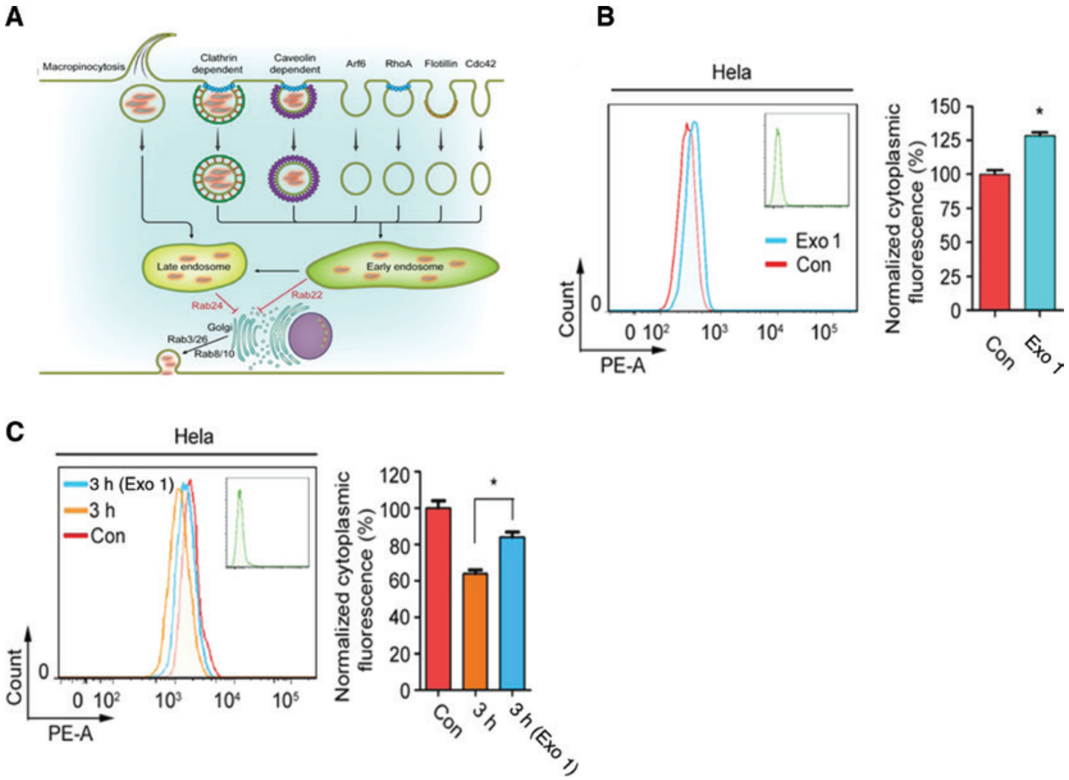

Figure 7: Increased accumulation of NSs within cells via exocytosis inhibition.
(A) Schematic diagram of intracellular trafficking pathways of WS_2 NSs in HeLa cells. (B) HeLa cells were pretreated with the exocytosis inhibitor Exo1 for 2 h, followed by another 3 h of incubation with WS_2-PEG/RB NSs. Then flow cytometry was used to quantify cytoplasmic fluorescence. (C) HeLa cells were first incubated with WS_2-PEG/RB NSs for 3 h, followed by another 2 h of Exo1 treatment. Then the medium was refreshed and the cells were kept in the culture for another 3 h. Flow cytometry was used to quantify cytoplasmic fluorescence.

reported pathways of MoS_2-PEG NSs [27], which could be attributed to the following: (1) The composition difference of NSs has little influence on their pathways and/or (2) the PEGylation effect covers up the composition difference of 2D NSs. Then, we moved on to further check whether the exocytosis inhibition strategy could also improve the therapeutic efficacy (photothermal therapeutic outcomes) of WS_2 NS-based PTAs (with a low dose of WS_2 NSs and under NIR laser with low power) as a universal method for combination cancer therapy. Therefore, Exo1 inhibitors were used to increase the accumulation of WS_2 NSs in tumor cells. In order to analyze the biocompatibility of Exo1, the cell viability was first tested after incubating the cells with Exo1 at a different dose. As displayed in Figure S16, there was no significant cytotoxicity for both cell lines at our tested dose, suggesting good biocompatibility and suitability for biomedical applications. After the confirmation of Exo1 biocompatibility, different treatments were performed: (1) saline, (2) Exo1, (3) Exo1 + NIR, (4) WS_2-PEG NSs, (5) WS_2-PEG NSs + NIR, and (6) WS_2-PEG NSs + Exo1 + NIR at different time points. Figure 8B,C indicates that the cells with treatments (1–4) show nearly no toxicity as a result of the low dosage and good biocompatibility of WS_2-PEG NSs and Exo1. For the PTT treatment groups, pretreated cells with Exo1 showed much more obvious therapeutic effect (e.g. 47.14% and 41.52% of viability) even at 0.5 W cm^{-2} (a low NIR power density) compared to that without Exo1 treatment (e.g. 66.75% and 63.22% at the same test level). With Exo1 treatment, although the same amount of mild heat was generated by the WS_2 NS-based PTAs at the same low concentration, the high accumulation of PTAs contributed more directly to damaging the intracellular organelles and proteins. This explains the reason why enhanced photothermal therapeutic outcomes were observed in the groups pretreated with Exo 1. On the contrary, without the incubation of Exo1, a certain amount of WS_2-PEG NSs would be expelled out of the cells via exocytosis, so that the generated heat could not directly harm the organelles and proteins in the cytoplasm due to the protection provided by the cell membranes, which is also consistent with our previous report [27]. Therefore, the exocytosis inhibition strategy was confirmed *in vitro* for WS_2 NS-based PTAs, which achieved remarkable therapeutic benefits at a lower WS_2

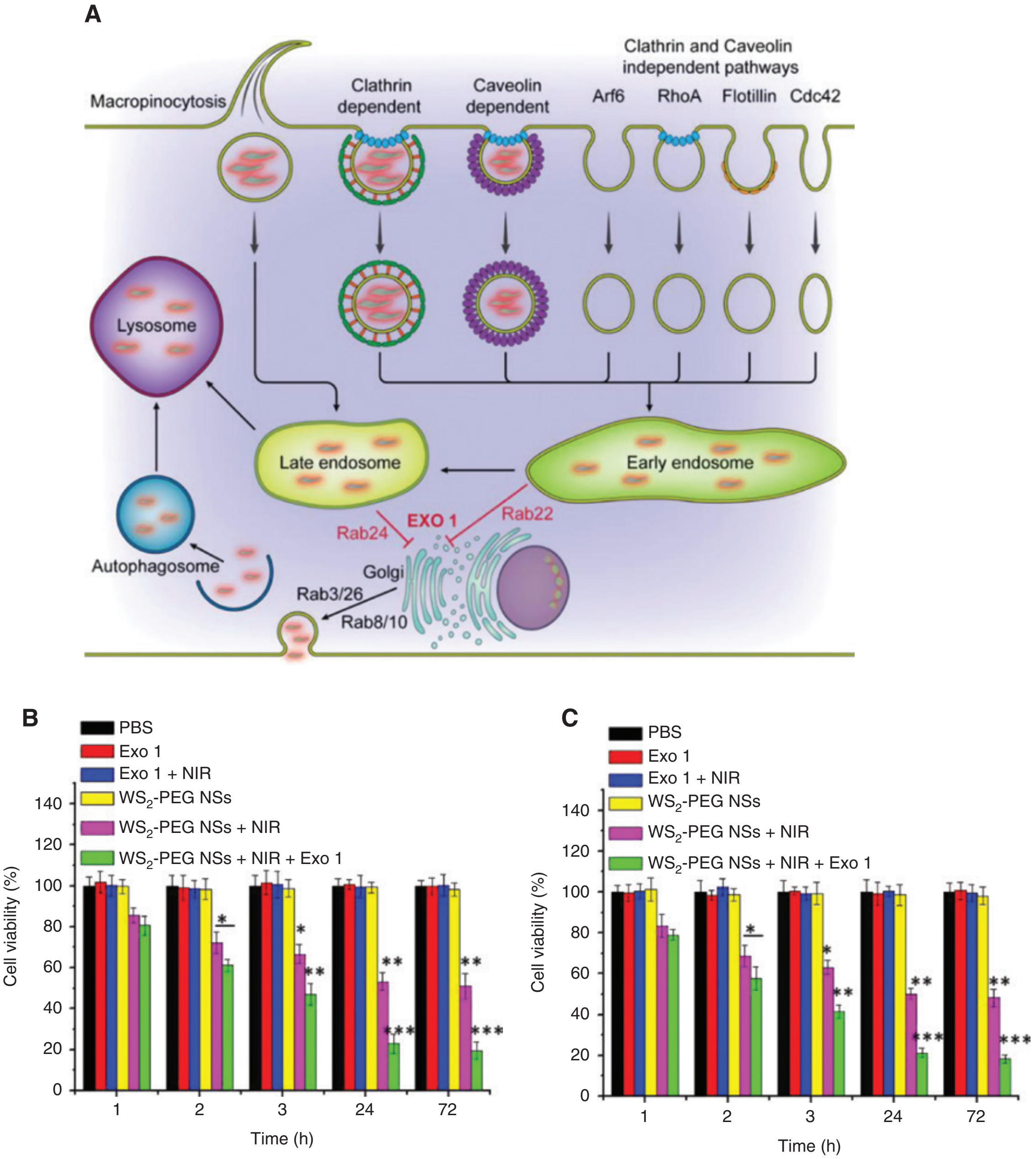

Figure 8: (A) Summary of the intracellular fate of WS_2 NSs. Cell viability of (B) HeLa cells or (C) MCF-7 cells after the following treatments at different time points: (1) PBS, (2) Exo1, (3) Exo1 + NIR, (4) WS_2-PEG NSs, (5) WS_2-PEG NSs + NIR, (6) WS_2-PEG NSs + Exo1 + NIR. The concentration of WS_2 was 100 µg ml^{-1}, while that of Exo1 was 50 µg ml^{-1}. NIR irradiation was conducted at the power density of 0.5 W cm^{-2} (5 min). MTT assay was used to determine the cell viability.

concentration, lower power density, and shorter incubation time.

3.7.3 Enhanced photothermal therapeutic outcomes via blocking exocytosis *in vivo*

To further confirm the universality of the exocytosis inhibition strategy, *in vivo* animal studies were carried out to check the possibility of exocytosis inhibition-enhanced PTT as an effective treatment method. To assess the accumulation of WS_2-based NSs in tumors, Balb/c nude mice bearing MCF-7 breast tumors were intravenously injected with the WS_2-PEG/Cy5.5 NSs in the absence and presence of Exo1. As displayed in Figure 9A, not much fluorescence was observed at 1 h post injection either with or without Exo1 treatment. The fluorescence intensity gradually increased up to 24 h in the tumors, indicating

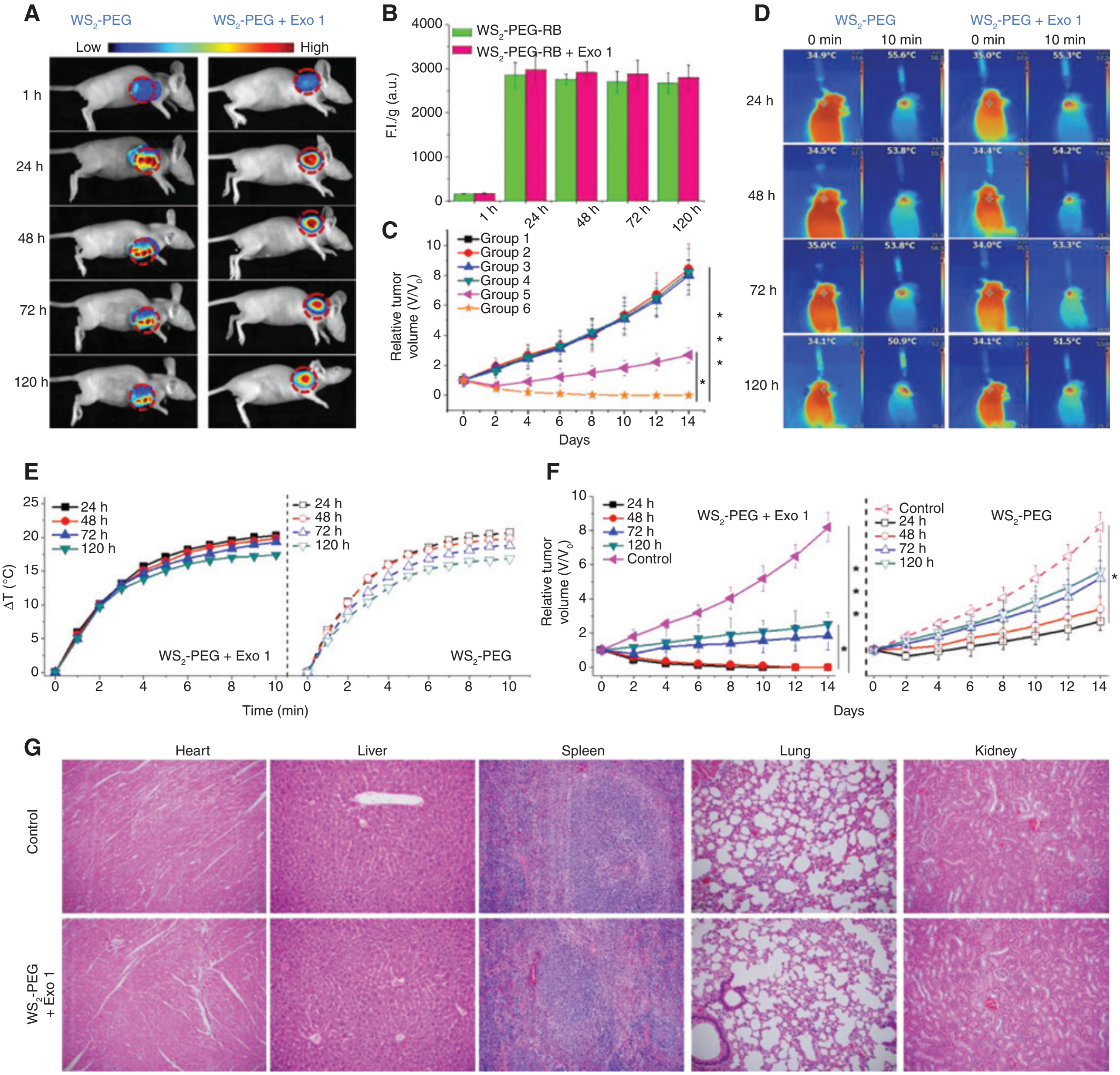

Figure 9: Enhanced photothermal therapeutic outcomes via blocking exocytosis *in vivo*.
(A) *Ex vivo* fluorescence images of the tumor sites were taken from mice treated with NSs at different time points. (B) Quantitative analysis of the NSs in the tumors. (C) Tumor growth curves of mice with different kinds of treatments. Group 1: saline; Group 2: WS_2-PEG NSs; Group 3: WS_2-PEG NSs + Exo1; Group 4: Exo1 + NIR; Group 5: WS_2-PEG NSs + NIR; Group 6: WS_2-PEG NSs + Exo1 + NIR (WS_2-PEG NSs: 6 mg kg^{-1}, intravenous injection; Exo1: 4 mg kg^{-1}, intratumoral injection). Twenty-four hours post injection, Groups 4, 5, and 6 were exposed to NIR radiation at tumor sites (808 nm, 0.5 W cm^{-2}, 10 min). (D) Photothermal images recorded by an IR thermal camera at a different time points. (E) Temperature changes at the tumor sites during the period of NIR irradiation. (F) Relative tumor volumes plotted between different groups. (G) H&E staining images of the major organs. Saline was used in the control group.

continuous WS_2 NSs accumulation at the tumor sites. Whether or not the WS_2-PEG/Cy5.5 NSs stayed inside the tumor cells or distributed in the intercellular space, due to the lack of effective lymphatic drainage of tumor tissues, they still dispersed at the tumor site. Hence, as shown in Figure 9A, even 120 h post injection, the tumor still showed a strong fluorescent signal (although decreased compared with that at 24 h post injection) either with or without Exo1 treatment. The tumors were collected at the determined time intervals after the injection of WS_2-PEG/Cy5.5 NSs. The samples were weighed and solubilized by a lysis buffer. Then the NS concentrations were measured by fluorometry in homogenized tissue lysates. As shown in Figure 9B, WS_2-PEG/Cy5.5 NSs reached the highest concentration 24 h post injection, and there was some decrease after 120 h post injection. Exo1 treatment showed negligible effect on the biodistribution of WS_2-PEG/Cy5.5 NSs in tumors.

Next, the MCF-7 breast tumor-bearing nude mice were treated with Group 1: saline (control group); Group 2: WS_2-PEG NSs; Group 3: WS_2-PEG NSs + Exo1; Group 4: Exo1 + NIR; Group 5: WS_2-PEG NSs + NIR; and Group 6: WS_2-PEG NSs + Exo1 + NIR. Twenty-four hours post injection, the tumor sites in Groups 4, 5, and 6 were exposed to NIR irradiation (808 nm, 0.5 W cm^{-2}, 10 min). After 10 min of irradiation, the tumor site temperature increase in Groups 4, 5, and 6 were 4.1, 20.7, and 20.3°C, respectively, which demonstrated that Exo1 had no photothermal effect and there was no obvious difference in temperature increase with or without Exo1 treatment. The tumor sizes were recorded and calculated every 2 days during the treatment. As shown in Figure 9C, Groups 2–4 showed a similar tumor-growth profile with respect to the control group. The tumor growth was suppressed in the WS_2-PEG NSs-treated group with laser irradiation (Group 5). More impressively, although there was nearly no difference in temperature increase between Groups 5 and 6, tumors were nearly eliminated in the mice treated with WS_2-PEG NSs + Exo1 followed by laser irradiation (Group 6). The enhanced therapeutic effect in Group 6 can be understood as follows: Exo1 enabled more WS_2-PEG NSs to accumulate inside the cancer cells, which generated more intracellular heat to directly damage tumor cell organelles and proteins (although the same level of total heat was produced as that with Exo1 treatment). On the contrary, without Exo1 treatment, some of these NSs could be expelled out of the tumor cells, which therefore could not directly contribute to the damage of organelles or proteins in the cytoplasm of these cells in the tumor site.

To confirm our speculation, Groups 5 and 6 were exposed to NIR after different times (i.e. 24, 48, 96, and 120 h) post injection. As shown in Figure 9E, after 10 min of irradiation, the tumor site temperature increase in Group 5 at 24, 48, 96, or 120 h post injection was 20.7, 19.3, 18.8, or 16.8°C, respectively. Those of Group 6 with Exo1 treatment maintained nearly the same temperature increase (20.3, 19.8, 19.3, or 17.4°C with irradiation after 24, 48, 96, or 120 h post injection, respectively). The tumor sizes were recorded and calculated every 2 days during the treatment. As presented in Figure 9F, the tumor inhibition effect of Group 5 (without Exo1) greatly decreased by prolonging the time interval between WS_2-PEG NSs injection and NIR irradiation. For Group 6 (with Exo1), Exo1 allowed more WS_2-PEG NSs accumulation inside the cancer cells, and even when exposed to NIR 48 h post injection, the tumors were nearly eliminated in the mice. There was still a very strong tumor inhibition effect 120 h post injection with Exo1 treatment. This result is consistent with the *in vitro* results, indicating that with Exo1 treatment, more WS_2-PEG NSs would accumulate within the cytoplasm of the tumor cells *in vitro* and the generated intracellular heat could more directly damage the organelles or proteins of the tumor cells. The survival ratios of Groups 5 and 6 were also detected, in which the mice in Group 6 showed a much longer average life span compared with those of Group 5 (Figure S17). Meanwhile, no observable effect on either the weight of the mice or tissue damage was detected in each group (Figures 9G and S18). This indicates that there are no acute side effects associated with this potential strategy.

4 Conclusions

In order to obtain the maximum therapeutic benefits as well as to limit their adverse health effects of 2D NS-based PTAs, comprehensive insights into their nano-bio interactions (especially the intracellular fate) are critical to fulfill their effective and safe biomedical application (e.g. PTT). Based on our previous studies on the intracellular fate of 2D MoS_2 NSs in cancer cells and their application in drug delivery platform-based anti-exocytosis-enhanced cancer treatment [27], we here aimed to reveal the detailed pathways of 2D WS_2 NS-based PTAs within the cancer cells, explore the influence of the composition difference on NSs' intracellular fate, and confirm whether the exocytosis inhibition strategy could be a universal one for other therapeutic modalities such as single PTAs to achieve combination cancer therapy. We had demonstrated that 2D WS_2 NS-based PTAs have a similar intracellular fate as 2D MoS_2 NS-based drug delivery platforms in our previous study, indicating that the composition difference of PEGylated NSs has little influence on the nano-bio interactions within cells. Moreover, the exocytosis inhibition strategy was further confirmed to be a universal treatment for NS-based PTAs, which can leads to effective combination therapy with a low dose of WS_2 NSs and under an NIR laser with low power. Through this fundamental study, we expect to provide a more systemic experimental basis of studies regarding the intracellular fate for the future development of 2D NSs in biomedicine.

Acknowledgments: N. K. and L. D. contributed equally to this work. This work was supported by the U.S. METAvivor Early Career Investigator Award (No. 2018A020560, W.T.), the Harvard Medical School/Brigham and Women's Hospital Department of Anesthesiology-Basic Scientist Grant (No. 2420 BPA075, W.T.), the National Natural Science Foundation of China (No. 81801826, Funder Id: http://dx.doi.org/10.13039/501100001809), and the Science, Technology and Innovation Commission of Shenzhen Municipality (No. JCYJ20180307153300735, Funder Id: http://dx.doi.org/10.13039/501100001809).

References

[1] Chen Y, Tan C, Zhang H, et al. Two-dimensional graphene analogues for biomedical applications. Chem Soc Rev 2015;44:2681–701.
[2] Li X, Shan J, Zhang W, et al. Recent advances in synthesis and biomedical applications of two-dimensional transition metal dichalcogenide nanosheets. Small 2017;13:1602660.
[3] Kurapati R, Kostarelos K, Prato M, et al. Biomedical uses for 2D materials beyond graphene: current advances and challenges ahead. Adv Mater 2016;28:6052–74.
[4] Agarwal V, Chatterjee K. Recent advances in the field of transition metal dichalcogenides for biomedical applications. Nanoscale 2018;10:16365–97.
[5] Ji X, Kang Y, Ouyang J, et al. Synthesis of ultrathin biotite nanosheets as an intelligent theranostic platform for combination cancer therapy. Adv Sci 2019;6:1901211.
[6] Ouyang J, Feng C, Ji X, et al. 2D monoelemental germanene quantum dots: synthesis as robust photothermal agents for photonic cancer nanomedicine. Angew Chem Int Ed 2019;131:13539–44.
[7] Tao W, Kong N, Ji X, et al. Emerging two-dimensional monoelemental materials (Xenes) for biomedical applications. Chem Soc Rev 2019;48:2891–912.
[8] Qiu M, Ren WX, Jeong T, et al. Omnipotent phosphorene: a next-generation, two-dimensional nanoplatform for multidisciplinary biomedical applications. Chem Soc Rev 2018;47:5588–601.
[9] Qiu M, Singh A, Wang D, et al. Biocompatible and biodegradable inorganic nanostructures for nanomedicine: silicon and black phosphorus. Nano Today 2019;25:135–55.
[10] Luo M, Fan T, Zhou Y, et al. 2D black phosphorus-based biomedical applications. Adv Funct Mater 2019;29:1808306.
[11] Fan T, Zhou Y, Qiu M, et al. Black phosphorus: a novel nanoplatform with potential in the field of bio-photonic nanomedicine. J Innov Opt Heal Sci 2018;11:1830003.
[12] Sun Z, Xie H, Tang S, et al. Ultrasmall black phosphorus quantum dots: synthesis and use as photothermal agents. Angew Chem Int Ed 2015;54:11526–30.
[13] Qiu M, Wang D, Liang W, et al. Novel concept of the smart NIR-light-controlled drug release of black phosphorus nanostructure for cancer therapy. Proc Natl Acad Sci USA 2018;115:501–6.
[14] Zhao J, Zhu J, Cao R, et al. Liquefaction of water on the surface of anisotropic two-dimensional atomic layered black phosphorus. Nat Commun 2019;10:4062.
[15] Pei J, Yang J, Yildirim T, et al. Many-body complexes in 2D semiconductors. Adv Mater 2019;31:1706945.
[16] Chen H, Liu T, Su Z, et al. 2D Transition metal dichalcogenide nanosheets for photo/thermo-based tumor imaging and therapy. Nanoscale Horiz 2018;3:74–89.
[17] Chhowalla M, Liu Z, Zhang H. Two-dimensional transition metal dichalcogenide [TMD] nanosheets. Chem Soc Rev 2015;44:2584–6.
[18] Shah P, Narayanan TN, Li CZ, et al. Probing the biocompatibility of MoS_2 nanosheets by cytotoxicity assay and electrical impedance spectroscopy. Nanotechnology 2015;26:315102.
[19] Zhe TW, Khim CEL, Zdeněk S, et al. Cytotoxicity of exfoliated transition-metal dichalcogenides [MoS_2 WS_2 and WSe_2] is lower than that of graphene and its analogues. Chem Eur J 2014;20:9627–32.
[20] Hao J, Song G, Liu T, et al. *In vivo* long-term biodistribution excretion and toxicology of PEGylated transition-metal dichalcogenides MS_2 [M=Mo W Ti] nanosheets. Adv Sci 2017;4:1600160.
[21] Mao J, Chen P, Liang J, et al. Receptor-mediated endocytosis of two-dimensional nanomaterials undergoes flat vesiculation and occurs by revolution and self-rotation. ACS Nano 2016;10:1493–502.
[22] Mahmoudi M, Bertrand N, Zope H, et al. Emerging understanding of the protein corona at the nano-bio interfaces. Nano Today 2016;11:817–32.
[23] Rosenblum D, Joshi N, Tao W, et al. Progress and challenges towards targeted delivery of cancer therapeutics. Nat Commun 2018;9:1410.
[24] Shi J, Kantoff PW, Wooster R, et al. Cancer nanomedicine: progress challenges and opportunities. Nat Rev Cancer 2017;17:20–37.
[25] Behzadi S, Serpooshan V, Tao W, et al. Cellular uptake of nanoparticles: journey inside the cell. Chem Soc Rev 2017;46:4218–44.
[26] Ding L, Zhu X, Wang Y, et al. Intracellular fate of nanoparticles with polydopamine surface engineering and a novel strategy for exocytosis-inhibiting lysosome impairment-based cancer therapy. Nano Lett 2017;17:6790–801.
[27] Zhu X, Ji X, Kong N, et al. Intracellular mechanistic understanding of 2D MoS_2 nanosheets for anti-exocytosis-enhanced synergistic cancer therapy. ACS Nano 2018;12:2922–38.
[28] Tao W, Zhu X, Yu X, et al. Black phosphorus nanosheets as a robust delivery platform for cancer theranostics. Adv Mater 2017;29:1603276.
[29] Tao W, Ji X, Zhu X, et al. Two-dimensional antimonene-based photonic nanomedicine for cancer theranostics. Adv Mater 2018;30:1802061.
[30] Tao W, Ji X, Xu X, et al. Antimonene quantum dots: synthesis and application as near-infrared photothermal agents for effective cancer therapy. Angew Chem Int Ed 2017;56:11896–900.
[31] Liang C, Jingjing L, Xing G, et al. PEGylated WS_2 nanosheets as a multifunctional theranostic agent for *in vivo* dual-modal CT/photoacoustic imaging guided photothermal therapy. Adv Mater 2014;26:1886–93.
[32] Stenmark H. Rab GTPases as coordinators of vesicle traffic. Nat Rev Mol Cell Biol 2009;10:513.
[33] Miserey-Lenkei S, Chalancon G, Bardin S, et al. Rab and actomyosin-dependent fission of transport vesicles at the golgi complex. Nat Cell Bio 2010;12:645.

[34] dos Santos T, Varela J, Lynch I, et al. Effects of transport inhibitors on the cellular uptake of carboxylated polystyrene nanoparticles in different cell lines. PLoS One 2011;6:e24438.

[35] Sarkar K, Kruhlak MJ, Erlandsen SL, et al. Selective inhibition by rottlerin of macropinocytosis in monocyte-derived dendritic. Cells Immunol 2005;116:513–24.

[36] Zhang X, Liang X, Gu J, et al. Investigation and intervention of autophagy to guide cancer treatment with nanogels. Nanoscale 2017;9:150–63.

[37] Zhang J, Zhang X, Liu G, et al. Intracellular trafficking network of protein nanocapsules: endocytosis exocytosis and autophagy. Theranostics 2016;6:2099–113.

[38] Bhuin T, Roy JK. Rab proteins: the key regulators of intracellular vesicle transport. Exp Cell Res 2014;328:1–19.

Supplementary Material: The online version of this article offers supplementary material (https://doi.org/10.1515/nanoph-2019-0343).